https://doi.org/10.5194/egusphere-2026-3195
Preprint. Discussion started: 22 July 2026

Meteorological and Land-Cover Controls on Grassland Fire Behaviour by WRF v4.4-SFIRE v0.1 with the computational optimization

Mengjie Lou[1], Qizhong Wu[1,2,*], Yongli Wang[3], Baogang Zhang[1,4], Jinhua Tao[5], Pu Gan[1], Huaqiong Cheng[1], Jiating Zhang[1], Jiahuan He[6], Meng Fan[5]

[1] Institute of Earth System Science, Faculty of Geographical Science, Beijing Normal University, Beijing, 100875, China
[2] College of Global and Earth System Science, Beijing Normal University, Beijing 100875, China
[3] National Institute of Natural Hazards, Ministry of Emergency Management of China, Beijing, 100085, China
[4] State Key Laboratory of Remote Sensing and Digital Earth, Beijing Normal University, Beijing, 100875, China
[5] The Aerospace Information Research Institute, Chinese Academy of Sciences, Beijing, 100094, China
[6] Hulun Buir Meteorological Bureau, Hulun Buir, 021008, China

Correspondence: Qizhong Wu (wqizhong@bnu.edu.cn)

Abstract

Under global warming, grassland wildfire risk has increased substantially. The WRF-SFIRE model was applied to the extreme grassland wildfire that occurred in Inner Mongolia in 2023, with satellite-derived fire perimeters used to evaluate the effects of meteorological forcing, land cover, and key driving factors on fire behavior, as well as to optimize model performance. For meteorological forcing, the FNL 6 h two-way coupling configuration achieved the highest spatial agreement with observations, with a recall of 39.1%, whereas ERA5 was more sensitive to short-term meteorological variability but tended to overestimate fire spread. For land cover, FROM_GLC30 (2017) showed relatively high overall agreement but tended to overexpand the fire, GlobeLand30 (2020) produced more conservative simulations, and GLC_FCS30D (2022) achieved the best overall performance. Fire-atmosphere feedback significantly enhanced fire spread rate and burned area. Wind speed exerted the strongest influence on burned area and spread distance, relative humidity mainly controlled spread rate and flame length, and air temperature played a secondary role. Among the fuel-related parameters, fuel load mainly affected flame intensity, fuel depth dominated burned area variation, and fuel moisture effects mainly regulated spread rate. In addition, the optimized computational configuration, particularly the combined use of PNetCDF and asynchronous I/O, reduced runtime by 29.3% relative to the baseline case. These results clarify the differential effects of input data and key driving factors on grassland fire behavior simulations and provide more reliable support for fire risk warning and

https://doi.org/10.5194/egusphere-2026-3195
Preprint. Discussion started: 22 July 2026

management.

1 Introduction

Grassland fire is a disturbance process in which combustible biomass ignites and spreads under favorable burning conditions after exposure to natural or anthropogenic ignition sources, causing varying degrees of damage to grassland ecosystems (Zhou et al., 2016). Under the combined effects of climate warming and increasing dry fuel loads, the global risk of grassland fire has intensified and is expected to further increase under future climate scenarios (Cao et al., 2024). Because of its rapid onset, fast spread, and the difficulty of suppression, grassland fire can cause substantial ecological, economic, and social losses, posing serious challenges to regional safety and emergency management. A better understanding of fire behavior is therefore essential for improving grassland fire response. Fire behavior describes the integrated characteristics of fire development from ignition to extinction, including burned area, rate of spread, flame height, residence time, fuel consumption, and fire intensity (Zhang et al., 2012). Grassland fire behavior is governed primarily by topography, fuel, and meteorological conditions (Ager et al., 2011). Among these factors, meteorological forcing is particularly important because of its strong spatiotemporal variability and its dynamic interaction with fire evolution. Fire-induced plume rise and associated inflow can in turn modify near-surface winds and alter the rate and direction of fire spread. However, traditional remote sensing products mainly provide static fire information and are limited in their ability to resolve the dynamic evolution of fire behavior because of constraints in temporal resolution, spatial resolution, and timeliness. These limitations reduce their utility for real-time fire analysis and emergency response. Fire spread models provide an effective alternative by explicitly simulating the key physical and chemical processes involved in fire propagation, thereby supporting more accurate identification of high-risk areas and more informed decisions in fire management and resource allocation.

Depending on whether fire-atmosphere interactions are represented, fire spread models can be broadly divided into uncoupled and coupled models. Uncoupled models, such as BEHAVE and other empirical or semi-empirical fire spread models, typically represent combustion using simplified energy-balance equations, combustion assumptions, or relationships derived from laboratory and point-ignition experiments, while treating meteorological variables as prescribed external forcing. This framework is computationally efficient and flexible in its input requirements, but it cannot represent feedbacks from the fire to the atmosphere (Burgan and Rothermel, 1984; Wang, 1992; Linn et al., 2002; Li, 2023). Coupled models, such as CAWFE, ARPS/DEVS-FIRE, HIGRAD/FIRETEC, and WRF-Fire (WRF-SFIRE), address this limitation by explicitly representing two-way fire-atmosphere interactions. At each time step, heat and moisture fluxes calculated by the fire module are passed to the atmospheric model, allowing the coupled evolution of fire and atmosphere to be resolved more realistically (Clark et al., 2004; Patton and Coen, 2004; Hu et al., 2012; Kochanski et al., 2013; Yang and Dong, 2020). Among these models, WRF-SFIRE has

https://doi.org/10.5194/egusphere-2026-3195
Preprint. Discussion started: 22 July 2026

several advantages. It is built on the mature Weather Research and Forecasting (WRF) framework, incorporates the Rothermel spread model in a flexible way, and uses a level-set method to represent fire spread and two-way fireline-atmosphere feedback on high-resolution grids. These features make it well suited for simulating fire-induced circulation, plume development, and their influence on spread pathways over complex terrain (Cheung et al., 2025). WRF-SFIRE has therefore been widely used in fire behavior studies, emergency response support, and studies of interactions between fire and the boundary layer. For example, in a complex terrain fire, the model successfully reproduced the dynamic interaction between wind and the fire front during the Xintian forest fire in Hunan Province, highlighting the key role of topographic forcing in shaping fire spread pathways (Hu et al., 2024). It has also been shown to capture mesoscale circulations generated by fire-atmosphere feedbacks. In simulations of the Bridger Foothills Fire in Montana, WRF-SFIRE reproduced lateral spread associated with a fire-induced vortex, improving understanding of coupled fire-atmosphere processes (Cheung et al., 2025). In addition, evaluation against the FireFlux II experimental burn showed that the two-way coupled framework improved the simulation of convergent flow near the fire head and the rate of spread compared with conventional one-way coupled approaches (Benik et al., 2023). By further coupling WRF-SFIRE with WRF-Chem, the WRF-SFIRE-Chem (WRFSC) model has been developed, making it possible to simulate fire emissions, aerosol radiative effects, and ozone chemistry simultaneously (Mallia et al., 2025).

However, the application of WRF-SFIRE to grassland fire remains constrained by two major challenges. One is the uncertainty associated with the choice of meteorological forcing and land-cover input data. The other is the high computational cost of high-resolution simulations, which limits both operational application and large-sample sensitivity analysis. To address these issues, this study investigates three aspects of WRF-SFIRE performance: input data, controlling factors, and computational efficiency. We first evaluate different combinations of meteorological reanalysis and land-cover datasets to identify the most suitable input configuration for the study area and reduce simulation uncertainty. We then conduct controlled experiments to assess the sensitivity of key fire-behavior metrics, including burned area, rate of spread, spread distance, and flame length, to major meteorological variables and fuel properties. Finally, we examine several approaches for improving computational efficiency, including compiler selection, parallel strategy, domain decomposition, and I/O optimization. The overall aim is to improve the applicability of WRF-SFIRE for grassland fire simulation and to provide more reliable support for fire risk assessment, early warning, and emergency response.

2 Data and methods

2.1 Case and domain configuration

This study examines an extreme grassland fire that occurred at 07:30 UTC on 1 May 2023 in Prairie Chenbarhu Banner, Hulunbuir, Inner Mongolia, China (approximately 119.09°E, 49.20°N). The observed burned extent was delineated from

https://doi.org/10.5194/egusphere-2026-3195
Preprint. Discussion started: 22 July 2026

pre-fire and post-fire remote sensing images (Fig. 1). The pre-fire image was a Level-1A radiometrically calibrated scene acquired by the Wide Field of View (WFV) sensor onboard GF-6 on 26 April 2023, whereas the post-fire image was a Level-1A radiometrically calibrated scene acquired by the Wide Field of View 1 (WFV1) sensor onboard GF-1 on 10 May 2023. Both images had a spatial resolution of 16 m. The burned area was initially extracted using the Burned Area Index (BAI) and subsequently refined through visual interpretation to improve boundary accuracy. The final burned area extended from approximately 118.76°E to 119.58°E and from 49.20°N to 50.00°N, with a total burned area of about 129,900 ha.

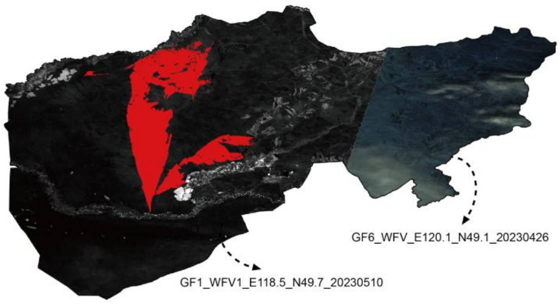

Fig. 1. Observed burned extent of the 1 May 2023 grassland fire.

The fire occurred over relatively flat terrain, with slopes of 3°-5°, and the surface vegetation was dominated by graminoid grasses. However, fuel distribution near the ignition area showed marked spatial heterogeneity. In some areas, hay harvesting in the previous year had reduced grass height to only 5-20 cm, whereas in undisturbed areas the grass height reached 60-70 cm, producing a pronounced gradient in fuel availability. Weather conditions on the day of the fire were highly favorable for rapid fire spread. Skies were clear, no precipitation had occurred during the previous 7 days, and relative humidity was as low as 12%-13%. Under the influence of strong southeasterly winds, the mean wind speed recorded at the Hailar station (49.25°N, 119.7°E) was 9 m/s, whereas wind speeds over the fire area were estimated to be 14.9-15.4 m/s, with instantaneous wind speeds reaching 19 m/s (Zhou et al., 2025).

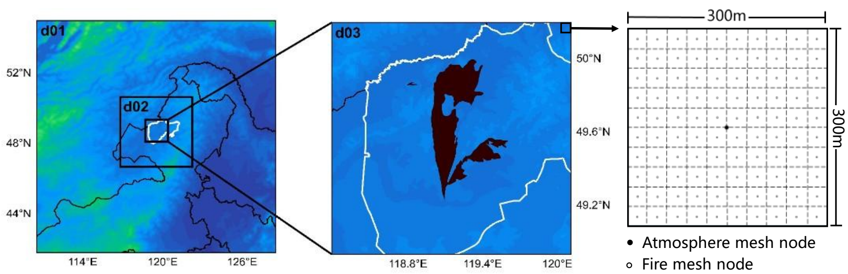

Fig. 2. Three-level nested domains and the fire case study area. The white outline indicates the boundary of Prairie Chenbarhu Banner, and the dark red area denotes the burned extent derived from remote sensing imagery.

A three-level nested grid system was used for the numerical simulations (Fig.

https://doi.org/10.5194/egusphere-2026-3195
Preprint. Discussion started: 22 July 2026

2．Three-level nested domains and the fire case study area. The white outline indicates the boundary of Prairie Chenbarhu Banner, and the dark red area denotes the burned extent derived from remote sensing imagery.). The three domains had horizontal resolutions of 7.5 km, 1.5 km, and 300 m, with 201, 301, and 471 grid points in both the west-east and south-north directions, respectively. All domains were configured with 46 vertical levels, and the model time step was set to 12 s. The parent-to-child grid ratio and time-step ratio were both set to 1:5:5. In the innermost domain, the fire mesh was refined to 30 m, which was 10 times finer than the atmospheric grid, to better resolve fireline processes and allow heat to be released progressively into the atmosphere (Hu et al., 2024). In addition, unlike WRF-Fire, which interpolates wind speed from 10 m to 6.096 m above ground level, WRF-SFIRE derives the near-surface wind used for fire spread from the lowest model level and interpolates it to 6.096 m. All results presented in this study are based on simulations from the innermost domain. The simulations covered the period from 00:00 to 18:00 UTC on 1 May 2023, with ignition initiated at 07:30 UTC in the model.

2.2 WRF-SFIRE configuration

The core modelling tool used in this study was the coupled WRF-SFIRE system, which explicitly represents the two-way feedbacks between fire spread and atmospheric dynamics. In this framework, WRF provides the background meteorological fields as a non-hydrostatic atmospheric model, whereas fire behavior is simulated by the SFIRE module based on a level-set method (Mandel et al., 2011, 2014). Fire spread is calculated using the Rothermel model with Anderson’s 13 fuel categories. Within the coupled system, near-surface winds simulated by WRF are interpolated to the high-resolution fire grid at each time step, and, together with terrain and fuel properties, drive fire propagation. At the same time, sensible and latent heat fluxes released by combustion are fed back into the atmospheric model, thereby dynamically modifying local meteorological conditions and enabling the full evolution of fire-atmosphere interactions to be represented. The main physical parameterization schemes are listed in Table 1. Large-eddy simulation (LES) was applied in the innermost domain to permit the explicit representation of turbulent eddies (Cheung et al., 2025).

Table 1. Physical parameterization schemes used in the WRF-SFIRE simulations.

Physics option	d01	d02	d03
Microphysics	WSM6 (Hong et al., 2004)		
Longwave radiation	RRTMG (Iacono et al., 2008)		
Shortwave radiation	Dudhia (Dudhia, 1989)		
Surface layer scheme	Revised Monin-Obukhov (Jiménez et al., 2012)		
Land surface model	Noah (Chen and Dudhia, 2001)		
PBL scheme	YSU (Hong and Lim, 2006)		/
Cumulus scheme	Kain-Fritsch (Kain, 2004)		/
Diffusion option	2nd-order diffusion		3D diffusion
Turbulence closure	Smagorinsky-Lilly closure (Lilly, 1962; Smagorinsky, 1963)		1.5-order TKE closure (Deardorff, 1980)

https://doi.org/10.5194/egusphere-2026-3195
Preprint. Discussion started: 22 July 2026

Note: / indicates that the corresponding scheme was not used.

2.3 Simulation accuracy improvement experiments

The simulation accuracy improvement experiments were conducted under otherwise identical conditions by varying the meteorological forcing and land cover datasets to quantitatively evaluate their effects on simulation results, such as burned area and fire spread rate. The meteorological forcing datasets used in this study were the NCEP Final Operational Global Analysis (FNL) and the ECMWF Reanalysis v5 (ERA5) (National Centers for Environmental Prediction et al., 2015; Hersbach et al., 2020). Both datasets had a spatial resolution of 0.25°, with temporal resolutions of 6 h for FNL and 1 h for ERA5. The experimental settings for different meteorological forcing conditions are summarized in Table 2.

Table 2. Configurations of meteorological forcing schemes in the simulation accuracy improvement experiments.

Meteorological forcing dataset	Temporal resolution	Spatial resolution	Fire-atmosphere two-way coupling
FNL	6h		FD
FNL	6h		noFD
ERA5	1h	0.25°	FD
ERA5	1h		noFD
ERA5	3h		FD

Note: FD indicates that fire-atmosphere two-way coupling was enabled, whereas noFD indicates that fire-atmosphere two-way coupling was disabled. ERA5 3 h denotes the forcing scheme in which the original 1 h ERA5 data were ingested into the model at 3 h intervals.

Three 30 m global land cover products were selected to construct fuel spatial distributions and perform comparative analyses: FROM-GLC (2017), GlobeLand30 (2020), and GLC_FCS30D (2022). FROM-GLC (2017) was released by the Tsinghua University team and generated based on the fusion and classification of multi-source medium- and high-resolution remote sensing imagery (Gong et al., 2019). GlobeLand30 (2020) was released by the National Geomatics Center of China and developed primarily from Landsat imagery, with the integration of other remote sensing data such as HJ-1 and GF-1 (Chen et al., 2015, 2021). GLC_FCS30D (2022), released by the Aerospace Information Research Institute, Chinese Academy of Sciences, is a 30 m dynamic land cover product developed using a continuous change detection approach. It contains 35 detailed land cover classes and can better characterize vegetation dynamics and their influence on fuel continuity (Zhang et al., 2024). To ensure comparability among the datasets, all three land cover products were reclassified, resampled, and reprojected in ArcGIS Pro to unify their spatial resolution and coordinate reference system. Because the fire module in WRF-SFIRE uses the Anderson 13 fuel model as the standardized fuel library (Anderson, 1982), all land cover types in the study area were converted into fuel categories recognizable by the model prior to simulation (Lai et al., 2020; Wang et al., 2023; Liu et al., 2024).

https://doi.org/10.5194/egusphere-2026-3195
Preprint. Discussion started: 22 July 2026

Accordingly, separate fuel mapping relationships were established for the three land cover datasets to generate different fuel spatial distributions, and their effects on fire behavior simulations were further evaluated. Detailed fuel mapping schemes and the resulting fuel type distributions are provided in Supplementary Material. The experimental settings for different land cover datasets are summarized in Table 3.

Table 3. Configurations of land cover datasets and their fuel mapping schemes in the simulation accuracy improvement experiments.

Land cover dataset	Spatial resolution	Number of original land cover classes	Number of mapped fuel classes
FROM_GLC (2017)		10	4
GlobeLand30 (2020)	30m	10	4
GLC_FCS30D (2022)		35	9

2.4 Key driving factor identification experiments

The key driving factor identification experiments quantified effects of meteorological and fuel-related variations on fire behavior and identified dominant controls on fire spread. Under otherwise identical conditions, a single-factor perturbation approach was adopted, evaluating responses of burned area, fire spread rate, and fire spatial pattern. For meteorological sensitivity, wind speed, relative humidity, and air temperature were perturbed at multiple levels, uniformly over the entire domain and forcing period. Table 4 summarizes the corresponding schemes.

Table 4. Perturbation schemes of meteorological factors in the key driving factor identification experiments.

Parameter	Perturbation scheme	Unit	Description
Wind speed	±2, ±4	$m\cdot s^{-1}$	Wind speed decreased or increased by 2 and 4 $m\cdot s^{-1}$
Relative humidity	±5, ±10	%	Relative humidity decreased or increased by 5% and 10%
Air temperature	±2, ±4	℃	Air temperature decreased or increased by 2 and 4 °C

For fuel-related sensitivity, fuel load and depth were adjusted at multiple levels, with an additional experiment enabling the fuel moisture model for comparison. Corresponding settings are given in Table 5.

Table 5. Perturbation schemes of fuel-related factors in the key driving factor identification experiments.

Parameter	Perturbation scheme	Unit	Description
Fuel moisture model	Enable	/	Fuel moisture model enabled
Fuel load	×0.25/0.5/1.5/1.75	$kg\cdot m^{-2}$	Adjusted to 0.25, 0.5, 1.5, and 1.75 times the baseline value
Fuel depth	×0.25/0.5/1.5/1.75	m	Adjusted to 0.25, 0.5, 1.5, and 1.75 times the baseline value

https://doi.org/10.5194/egusphere-2026-3195
Preprint. Discussion started: 22 July 2026

2.5 Computational efficiency optimization experiments

The computational efficiency optimization experiments were designed to improve the runtime performance of large-scale WRF-SFIRE simulations and to support high-resolution fire behavior modelling with rapid computational turnaround. Based on the parallel computing framework shown in Fig. 3, this study systematically optimized WRF-SFIRE from both the software and parallel configuration perspectives, focusing on four aspects: compiler selection, parallel computing strategy, grid decomposition, and storage I/O optimization. All performance tests were conducted using the same wildfire case, with a simulation duration of 1 h. Each configuration was repeated three times, and the average runtime was used for analysis.

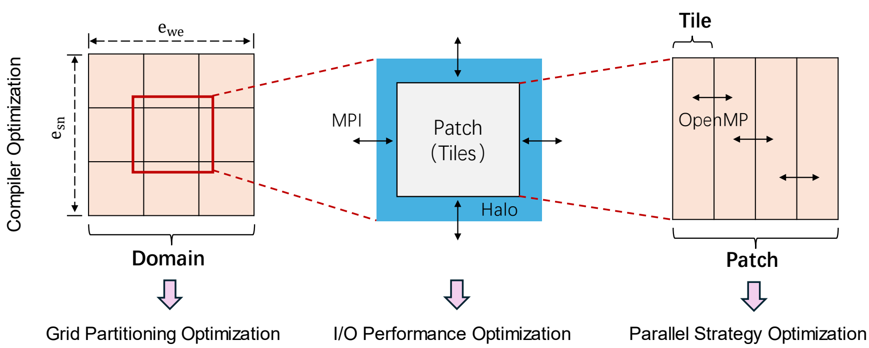

Fig. 3. Parallel computing framework and optimization workflow of WRF-SFIRE.

All numerical simulations and computational optimization tests were performed on a high-performance computing cluster. The hardware platform consisted of 12 compute nodes, each with dual Intel Xeon Gold 6148 processors (40 physical cores per node) and 32 GB DDR4-3200 MHz memory in a dual-channel NUMA architecture. A Lustre distributed file system supported large-scale I/O operations. The software environment was CentOS Linux 7, with compilation and parallel execution using the Intel compiler suite and Intel MPI library. Simulations used WRF v4.4 coupled with SFIRE v0.1, along with PnetCDF (v1.12.3), NetCDF-C (v4.9.0), and NetCDF-Fortran (v4.6.0).

The first optimization aspect focused on compiler selection. To assess the influence of different Intel compiler toolchains on the parallel performance of WRF-SFIRE, comparative tests were conducted using three compilation environments: Intel Parallel Studio XE 2018 with Intel MPI Library 2018 (v18), Intel OneAPI 2021.4.0 with Intel MPI Library 2021.4.0 (v21), and Intel OneAPI 2022.3.1 with Intel MPI Library 2021.7 (v22). The corresponding WRF-SFIRE compilation settings are provided in Supplementary Material.

The second aspect of the optimization focused on the parallel computing strategy. To compare the effects of different resource configurations on the runtime performance of WRF-SFIRE under pure MPI and MPI+OpenMP hybrid modes, parallel experiments were designed based on the relationships among the total number of CPU cores ($N_{core,total}$), the number of nodes (N_{node}), the number of MPI processes per node

https://doi.org/10.5194/egusphere-2026-3195
Preprint. Discussion started: 22 July 2026

($N_{MPI,node}$), and the number of OpenMP threads (N_{OMP}). Under the MPI mode, $N_{core,total} = N_{node} \times N_{MPI,node}$. On this basis, two groups of experiments were designed: one with fixed $N_{MPI,node}$, in which $N_{core,total}$ was adjusted by changing N_{node}, and the other with fixed N_{node}, in which $N_{core,total}$ was adjusted by changing $N_{MPI,node}$. Under the MPI+OpenMP hybrid mode, $N_{core,total} = N_{node} \times N_{MPI,node} \times N_{OMP}$. In this mode, $N_{core,total}$ and N_{node} were fixed, and the performance differences among hybrid parallel configurations were evaluated by varying the combinations of $N_{MPI,node}$ and N_{OMP}. Detailed descriptions of the two parallel modes are provided in Supplementary Material.

The third aspect of the optimization focused on grid decomposition. WRF-SFIRE adopts a two-dimensional MPI domain decomposition scheme (see Supplementary Material), in which the total number of MPI processes ($N_{MPI,total} = N_{node} \times N_{MPI,node}$) is decomposed into the number of MPI process partitions in the west-east direction ($N_{proc,x}$) and the south-north direction ($N_{proc,y}$). To ensure that each subdomain contains a sufficient number of interior grid cells for effective computation while controlling the communication overhead associated with subdomain boundaries, the process decomposition in each direction must satisfy $e_{we}/N_{proc,x} > 10$, $e_{sn}/N_{proc,y} > 10$. Here, e_{we} and e_{sn} denote the total numbers of grid cells in the west-east and south-north directions, respectively. Based on these constraints, and under fixed values of $N_{core,total}$ and N_{OMP}, comparative tests were conducted for different two-dimensional MPI decomposition combinations to identify a more efficient grid decomposition scheme.

The fourth aspect of the optimization focused on I/O optimization. WRF-SFIRE supports three main data I/O mechanisms: serial I/O (Serial NetCDF), parallel I/O (PNetCDF), and asynchronous I/O (Asynchronous I/O via Quilt Server). The relevant principles are described in Supplementary Material. When asynchronous I/O is enabled, the total number of I/O processes ($N_{I/O}$) is the product of the number of processes in each I/O group ($N_{I/O,task}$) and the number of I/O groups ($N_{I/O,group}$). In this case, the total number of MPI processes satisfies $N_{MPI,total} = N_{proc,x} \times N_{proc,y} + N_{I/O}$. Based on this, this study compared the performance differences among serial I/O, parallel I/O, asynchronous I/O, and PNetCDF combined with asynchronous I/O, and further evaluated their effects on model runtime efficiency from two aspects: asynchronous I/O process ratio and grouping strategy. The detailed experimental settings are listed in Table 6.

Table 6. Experimental settings for I/O optimization.

I/O mode	Control condition
Serial I/O	NetCDF enabled
Parallel I/O	PNetCDF enabled
Parallel I/O	NetCDF enabled, fixed $N_{I/O,task}$
	NetCDF enabled, fixed $N_{I/O}$
Asynchronous I/O + Parallel I/O	PNetCDF enabled, fixed $N_{MPI,total}$

https://doi.org/10.5194/egusphere-2026-3195
Preprint. Discussion started: 22 July 2026

3 Results and discussion

3.1 Simulation accuracy under different input datasets

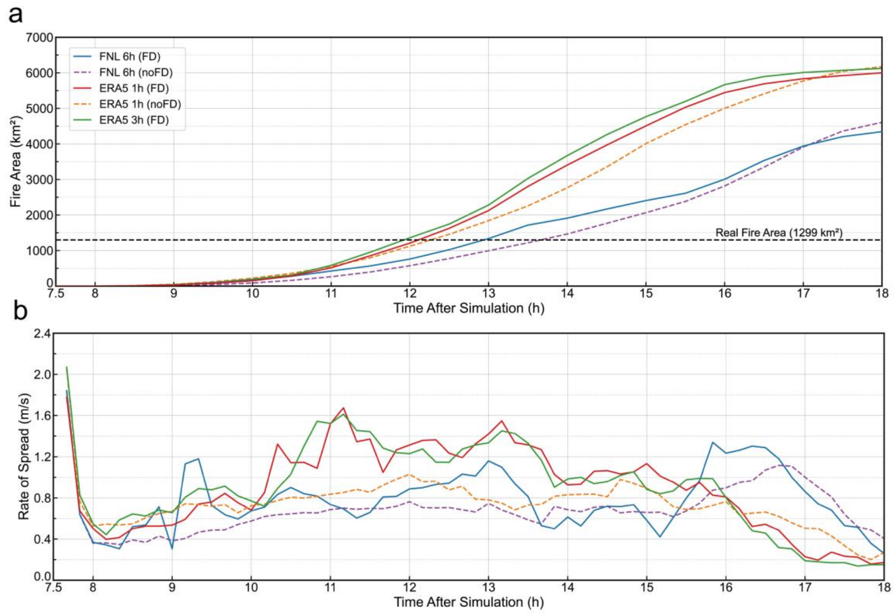

Fig. 4. Time series of burned area and fire spread rate under different meteorological forcing scenarios. FD and noFD indicate simulations with and without fire-atmosphere two-way coupling. The horizontal dashed line in panel (a) marks the observed burned area (1299 km^2) based on field investigation.

For the meteorological forcing experiments, clear differences are found in both the temporal evolution and spatial pattern of fire spread among the scenarios. As shown in Fig. 4, the burned area increases continuously in all scenarios after ignition at 7.5 h, indicating a strong potential for sustained spread of grassland fire in the absence of human intervention. Under the same meteorological forcing, the FD scenarios show more pronounced acceleration after approximately 12 h, whereas the noFD scenarios exhibit a more gradual increase. However, during the later stage of the simulation (>17 h), the burned area in the noFD scenarios exceeds that in the FD scenarios. This difference may be associated with the real-time feedback in the FD scenarios, which modifies the local wind field and thermal structure, thereby limiting further fire expansion. In contrast, the absence of this process in the noFD scenarios allows the influence of the background meteorological forcing to persist. Under the same coupling configuration, the ERA5-driven scenarios generally produce larger burned areas and higher spread rates than the FNL-driven scenarios, indicating that meteorological forcing with higher temporal resolution is more favorable for representing fire spread.

https://doi.org/10.5194/egusphere-2026-3195
Preprint. Discussion started: 22 July 2026

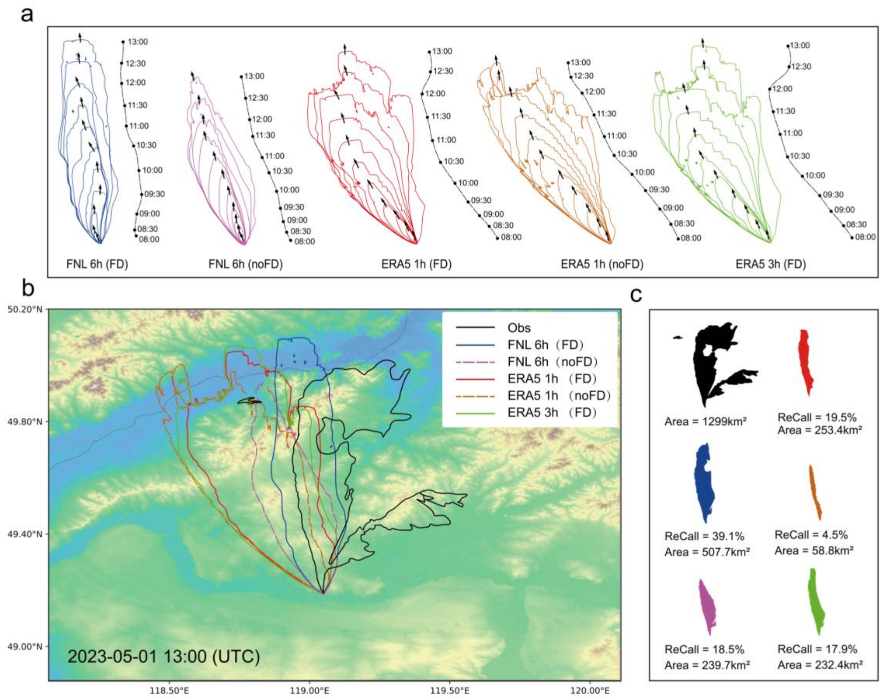

Fig. 5. Spatial differences in burned area under different meteorological forcing scenarios. (a) Simulated fire perimeters at 30 min intervals from 08:00 to 13:00 UTC, with arrows indicating the direction of fire-front propagation. (b) Comparison of simulated and observed burned-area perimeters at 13:00 UTC. (c) Simulated burned areas and Recall values at 13:00 UTC, where Recall is defined as the ratio of the overlapping area to the total observed burned area.

Fig. 5 further illustrates differences in fire spread under different meteorological scenarios. Overall, the ERA5-driven scenarios show faster expansion and stronger northwestward spread, resulting in a more pronounced outward extension. In contrast, the FNL-driven scenarios produce more confined fire perimeters, with spread directions closer to the observed pattern. Further comparison indicates that the ERA5-driven scenarios consistently exhibit excessive expansion on the northwestern side, whereas the FNL-driven scenarios better constrain the fire extent. Under both meteorological forcings, the noFD scenarios show a more uniform spread direction, indicating stronger control by the background meteorological forcing in the absence of two-way fire-atmosphere feedback. By contrast, the FD scenarios more closely reproduce the observed fire geometry and spread pathway. Quantitatively, although the ERA5-driven scenarios produce larger burned areas, all Recall values remain below 20%, whereas FNL 6h (FD) achieves the highest Recall of 39.1% (507.7 km^2), indicating the best agreement with the observed burned area in both extent and location.

https://doi.org/10.5194/egusphere-2026-3195
Preprint. Discussion started: 22 July 2026

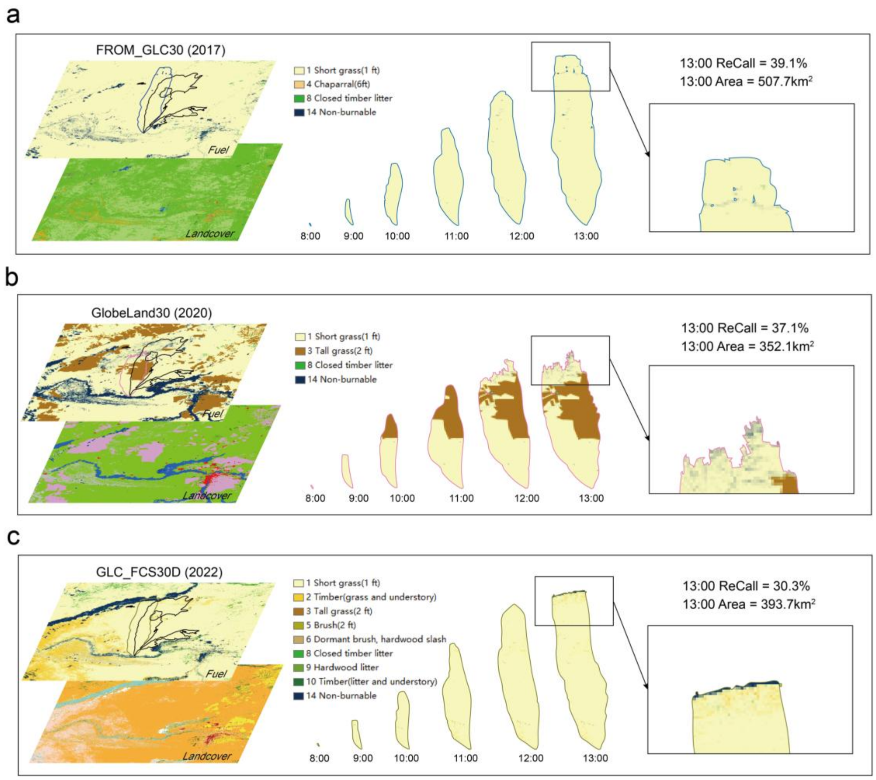

Fig. 6. Spatial differences in burned area under different fuel distribution scenarios. Land-cover classes are shown using the official color schemes of the corresponding datasets, whereas fuel types are displayed according to the standard color scheme of the Anderson 13 fuel models.

For the land-cover experiments, Fig. 6 shows the spatial differences in burned area among the three fuel distribution scenarios. In Fig. 6a, the FROM_GLC30 (2017) scenario is dominated by short grass fuel, with a relatively homogeneous fuel distribution, and the fire spread generally follows a linear pattern along the prevailing wind direction. However, this dataset fails to adequately identify the wetland and marsh areas along the China-Russia border, causing some of these areas to be mapped as burnable short grass fuel and thereby leading to pronounced overexpansion when the fire spreads northward. Nevertheless, this scenario shows better overall spatial agreement with the observed burn scar than the other two scenarios. By contrast, the GlobeLand30 (2020) scenario shown in Fig. 6b exhibits a more complex fuel structure, in which tall grass fuel dominates the burned area. Because tall grass fuel is generally associated with higher fuel load and greater potential fire intensity, this scenario shows higher overall burn potential. However, the non-burnable areas are highly fragmented, creating local barriers to fire spread. As a result, the fire front is repeatedly deflected during propagation, producing a more irregular fire-head shape. At 13:00 UTC, the overlap area between the simulated and observed burned areas is 352.1 km^2, with a

https://doi.org/10.5194/egusphere-2026-3195
Preprint. Discussion started: 22 July 2026

Recall of only 27.1%. The GLC_FCS30D (2022) scenario shown in Fig. 6c has the most detailed fuel classification, including multiple fuel types such as low shrub, understory vegetation, and forest. Its overall spread pattern is similar to that of the FROM_GLC30 (2017) scenario, but it is able to identify fine-scale non-burnable patches along the spread pathway. These areas help limit excessive fire expansion to some extent, particularly near the fire head.

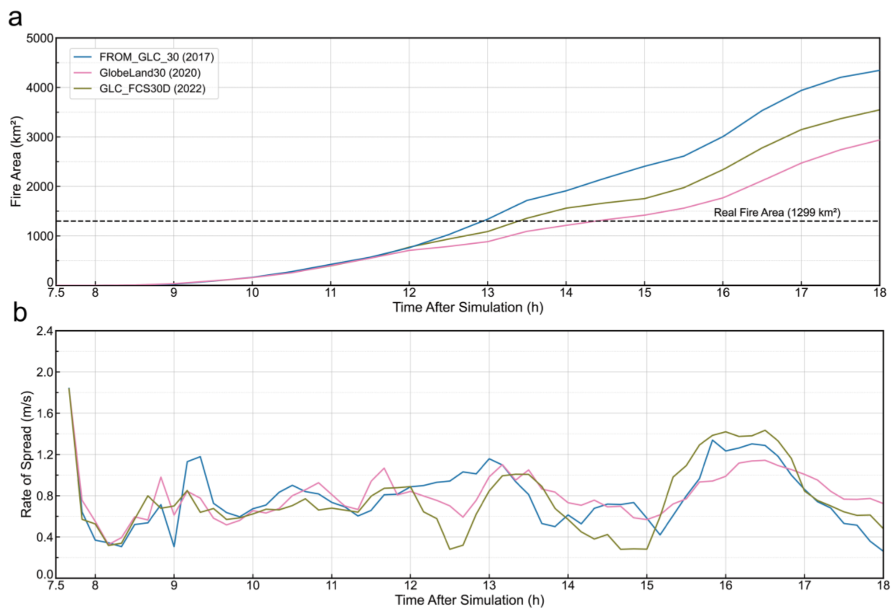

Fig. 7. Time series of burned area and fire spread rate under different fuel distribution scenarios.

As shown in Fig. 7a, differences in burned area among the three fuel distribution scenarios are not significant during the initial stage of the fire, indicating that fire spread at this stage is mainly controlled by meteorological conditions such as wind speed and humidity. However, as time progresses, the burned areas gradually diverge, with the overall ranking of FROM_GLC30 (2017) > GLC_FCS30D (2022) > GlobeLand30 (2020). This difference reflects the critical influence of fuel spatial structure, particularly the distribution and connectivity of non-burnable areas, on the later-stage extent of fire spread. In the fire spread rate curves shown in Fig. 7b, the three fuel distribution scenarios exhibit similar temporal patterns, suggesting that external meteorological factors still dominate the overall pace of fire spread. However, the GLC_FCS30D (2022) scenario shows a marked decrease in spread rate during 12–13 h of the simulation, which is related to the fire front encountering a relatively large non-burnable area. Overall, although meteorological conditions dominate the initial stage of fire spread, fuel spatial heterogeneity gradually controls the extent and dynamics of fire spread during the later stage, thereby significantly amplifying the simulation differences among the datasets.

https://doi.org/10.5194/egusphere-2026-3195
Preprint. Discussion started: 22 July 2026

3.2 Fire behavior responses to meteorological and fuel perturbations

Based on the preceding results, FNL 6h (FD) and FROM_GLC30 (2017) were selected as the baseline configuration for sensitivity experiments to identify the key driving factors. Four perturbation levels were then applied to wind speed (WS), relative humidity (RH), and air temperature (TT), and the results are shown in Fig. 8.

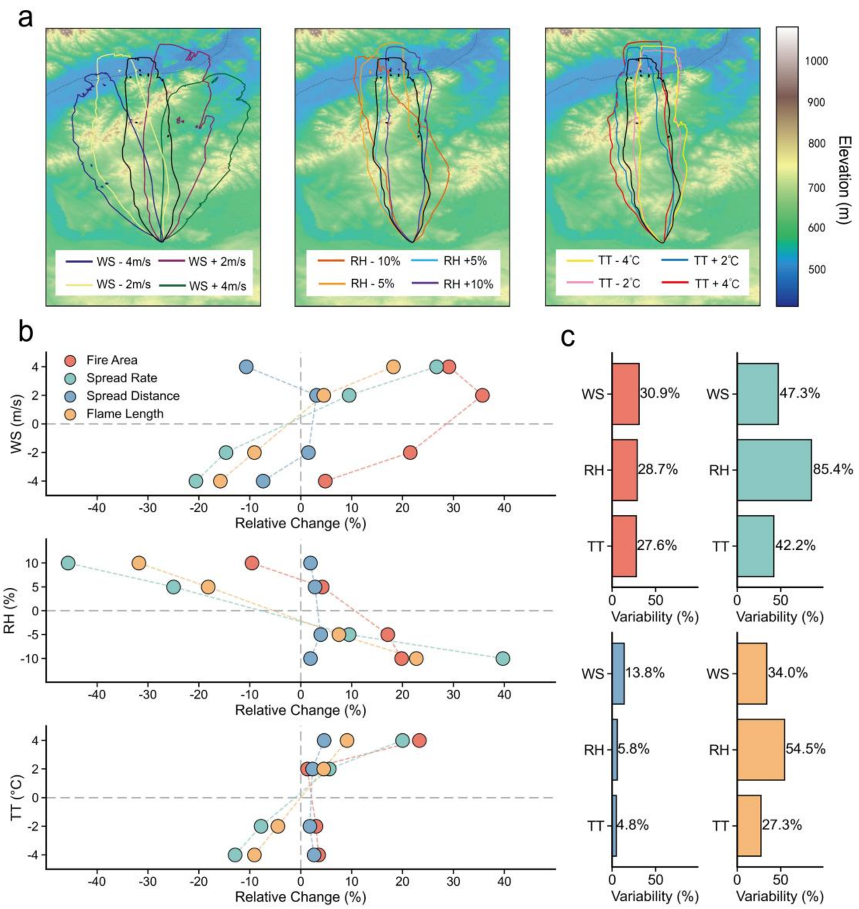

Fig. 8. Spatial variability and sensitivity of key fire-behavior parameters to meteorological factor perturbations.

Fig. 8a shows that WS perturbations produce the most pronounced spatial response. As WS increases, both the fire perimeter and the most advanced fire head shift markedly toward the northeast; as WS decreases, the main axis of the fire turns toward the northwest and shows a westward expansion. This indicates that WS perturbations can alter the dominant spread direction of the fire by modifying the near-surface wind forcing on the fire head and the relative effect of wind-slope coupling. By contrast, perturbations in RH and TT have weaker effects on the fire perimeter, and the burned areas remain more compact, extending mainly in the meridional direction. Fig. 8b further compares the responses of four key fire-behavior metrics to the three

https://doi.org/10.5194/egusphere-2026-3195
Preprint. Discussion started: 22 July 2026

meteorological perturbations. Burned area shows a consistent response across all perturbations, with increases in WS, decreases in RH, and increases in TT all leading to larger burned areas, indicating that stronger winds and warmer, drier conditions favor fire spread. Spread rate is most sensitive to RH, decreasing markedly as RH increases and increasing substantially as RH decreases, whereas the effects of WS and TT are comparatively weaker. Spread distance varies only slightly overall, suggesting a limited response to meteorological perturbations. Flame length shows an intermediate sensitivity, with stronger responses to RH and WS and a weaker response to TT. Fig. 8c further shows that the dominant meteorological controls vary among fire-behavior metrics. WS has the strongest effect on burned area and spread distance (30.9% and 13.8%), whereas RH shows the highest sensitivity for spread rate and flame length (85.4% and 54.5%). In contrast, TT shows the weakest overall sensitivity.

As shown in Fig. 9, additional perturbation experiments were performed for the fuel moisture model (fuelmc), fuel load (fgi), and fuel depth (fueldepthm) to quantify the relative responses of fire-behavior parameters to different fuel factor perturbations.

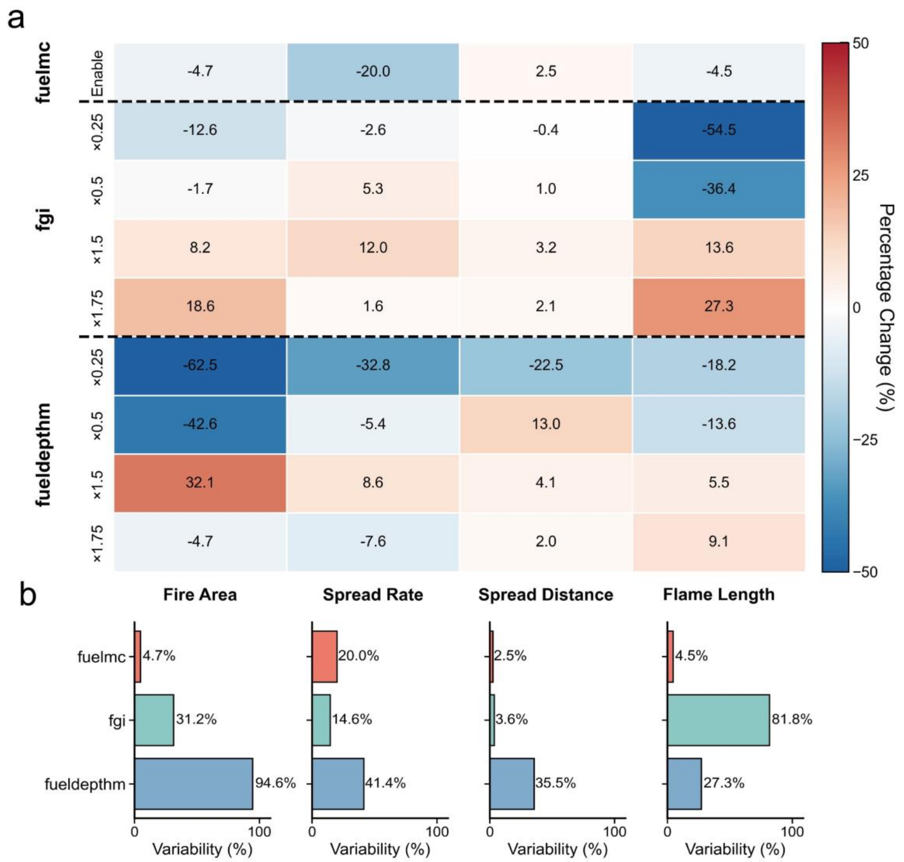

Fig. 9. Sensitivity of key fire-behavior parameters to fuel factor perturbations.

Fig. 9a shows that enabling fuelmc reduces burned area, spread rate, and flame

https://doi.org/10.5194/egusphere-2026-3195
Preprint. Discussion started: 22 July 2026

length by 4.7%, 20.0%, and 4.5%, respectively, while increasing spread distance by 2.5%. This indicates that the fuel moisture model mainly affects metrics related to fire intensity, with a relatively limited effect on spatial expansion. The dominant sensitivity analysis in Fig. 9b further indicates that the overall sensitivity of fuelmc is low. Under fgi perturbations, fuel load is positively correlated with flame length and burned area, with flame length showing the highest sensitivity and a variation range of 81.8%. When fgi increases to 1.75 times the baseline, flame length and burned area increase by 27.3% and 18.6%, respectively; when fgi decreases to 0.25 times the baseline, flame length and burned area decrease by 54.5% and 12.6%, respectively. By contrast, the effects of fgi on spread rate and spread distance are weaker, with variation ranges of 14.6% and 3.6%, respectively. Both metrics increase under moderate fuel loading, but this increase weakens under high fuel loading, indicating a nonlinear response. By comparison, fueldepthm shows a stronger nonlinear effect on fire behavior. When fueldepthm decreases to 0.25 times the baseline, burned area, spread rate, spread distance, and flame length decrease by 62.5%, 22.5%, 32.8%, and 18.2%, respectively, indicating strong suppression of both fire spread and fire intensity under shallow fuel conditions. As fueldepthm increases, fire spread capacity and intensity generally increase. However, when fueldepthm further increases to 1.75 times the baseline, flame length continues to increase, whereas the increases in the other metrics weaken or become suppressed. Fig. 9b further shows that fueldepthm has the strongest effect on burned area (94.6%), followed by spread rate.

3.3 Computational optimization strategies for WRF-SFIRE

Using the three Intel compiler toolchain configurations introduced earlier, the effects of compiler version on parallel performance of WRF-SFIRE were evaluated. The results showed that v18 produced the shortest runtime, at 17 min 39 s, whereas the runtimes of v21 and v22 were 18 min 04 s and 17 min 59 s, representing increases of 2.4% and 1.9%, respectively, relative to v18. Therefore, for complex numerical models such as WRF-SFIRE, the optimal compiler version should still be identified on the basis of targeted benchmarking under specific hardware and configuration settings.

Table 7. Effects of node scaling and process density configuration on the parallel efficiency of WRF-SFIRE under pure MPI mode.

Test Case	$N_{core,total}$	N_{node}	$N_{MPI,node}$	Runtime
Node scaling test	480	12	40	15m22s
	320	8		19m57s
	160	4		32m47s
	80	2		59m20s
Process density test	400*	10	40	17m39s
	360		36	17m11s
	320		32	18m12s
	300		30	19m12s

Note: * indicates the base case, and the same notation is used hereafter.

https://doi.org/10.5194/egusphere-2026-3195
Preprint. Discussion started: 22 July 2026

After identifying v18 as the optimal compiler toolchain, further experiments were conducted according to the settings listed in Table 7 to evaluate the effects of different resource configurations on the parallel efficiency of WRF-SFIRE under the pure MPI mode (Table 7). When $N_{MPI,node} = 40$, increasing N_{node} from 2 to 12 reduced the model runtime from 59m20s to 15m22s, indicating that increasing the number of nodes is an effective way to improve parallel performance. In contrast, when $N_{node} = 10$, reducing $N_{MPI,node}$ from 40 to 30 resulted in only limited runtime variation (17m39s-19m12s). The best performance was achieved with 36 MPI processes per node. Overall, cross-node scaling contributed more to performance improvement than adjusting per-node process density, and a per-node load of approximately 90%-95% was more favorable for mitigating intra-node resource contention.

Table 8. Effects of Different Parallel Configurations on the Parallel Performance of WRF-SFIRE.

Parallel mode	$N_{MPI,node}$	N_{OMP}	N_{node}	$N_{core,total}$	Runtime
MPI*	40	0	10	400	17m39s
MPI+OpenMP	20	2			15m43s
	10	4			15m06s
	5	8			18m43s

Based on the pure MPI tests, the performance advantage of the MPI+OpenMP hybrid parallel mode was further evaluated, and the results are presented in Table 8. The results show that, under a fixed total computational resource ($N_{core,total} = 400$), the hybrid parallel mode outperformed the pure MPI mode in most configurations, although its performance was sensitive to the combination of MPI processes and OpenMP threads. The best performance was obtained at $N_{MPI,node} = 10$ and $N_{OMP} = 4$, for which the runtime was reduced by approximately 14.5% relative to the pure MPI mode. This indicates that introducing an appropriate number of OpenMP threads while reducing the number of MPI processes can help decrease inter-process communication overhead and improve the utilizationefficiency of shared-memory resources within each node. However, when N_{OMP} was further increased to 8, the runtime increased markedly and even exceeded that of the pure MPI mode, suggesting that a higher thread count may introduce additional overhead associated with thread scheduling, synchronization, and memory access. Overall, the optimal MPI/OpenMP combination should be determined by specific hardware and model characteristics, and simply increasing threads does not necessarily improve parallel efficiency.

Table 9. Effects of grid decomposition on the parallel computational efficiency of WRF-SFIRE.

$N_{core,total}$	$N_{proc,x}$	$N_{proc,y}$	η	Runtime
120	6	20	2.33	22m02s
	8	15	0.88	22m48s
	10	12	0.20	24m30s
	12	10	0.20	25m02s
	15	8	0.88	26m43s
	20	6	2.33	29m20s

https://doi.org/10.5194/egusphere-2026-3195
Preprint. Discussion started: 22 July 2026

Note: η is the asymmetry index, defined as $\eta = \frac{|N_{proc,x} - N_{proc,y}|}{min(N_{proc,x}, N_{proc,x})}$, which quantifies the imbalance in MPI process allocation between the two directions. Larger η values indicate greater imbalance.

On the basis of the theoretical framework and quantitative criteria described in the previous section and Supplementary Material, the actual impact of grid decomposition strategy on the parallel computational efficiency of WRF-SFIRE was further evaluated. Under the constraints of the hardware configuration ($N_{node} \leq 12, N_{MPI,node} \leq 40$) and the model grid decomposition rules ($e_{we}/N_{proc,x} > 10,\ e_{\mathrm{sn}}/N_{proc,y} > 10$), the total number of parallel tasks was fixed at 120, and the results are shown in Table 9. When process allocation was dominant in one direction, highly asymmetric configurations exhibited higher computational efficiency than near-symmetric configurations. This finding contrasts with the communication-optimization preference commonly recommended in the WRF documentation, namely $N_{proc,x} \approx N_{proc,y}$, and suggests that WRF-SFIRE has its own specific requirements for process decomposition. In addition, the two highly asymmetric configurations with η = 2.33 showed markedly different performance. Specifically, the case with $N_{proc,x} = 6$ and $N_{proc,y} = 20$, indicating a larger number of processes in the north-south direction, achieved the shortest runtime (22m02s), whereas the case with $N_{proc,x} = 20$ and $N_{proc,y} = 6$, indicating a larger number of processes in the east-west direction, produced the longest runtime (29m20s). These results indicate that the parallel computational load of WRF-SFIRE is sensitive to directional decomposition. Allocating more processes in the north-south direction than in the east-west direction is therefore beneficial for optimizing the global communication pattern and computational load distribution, thereby improving overall computational efficiency.

Table 10. Effects of asynchronous I/O configurations on the parallel computational efficiency of WRF-SFIRE.

Test Case	$N_{I/O,task}$	$N_{I/O,group}$	$N_{I/O}$	I/O Ratio	$N_{core,total}$	Runtime
Asynchronous I/O process ratio	0*	1	0	0%	400	17m39s
	5	2	10	2.5%		16m20s
		4	20	5%		17m49s
		6	30	7.5%		16m02s
		8	40	10%		14m38s
		10	50	12.5%		13m49s
		12	60	15%		16m27s
		14	70	17.5%		17m54s
Asynchronous I/O task grouping	1	50	50	7.5%	400	/
	2	25				15m43s
	5	10				13m49s
	10	5				14m19s
	25	2				13m38s
	50	1				/

Note: Test cases for which valid integrated results could not be obtained are indicated by /.

On this basis, the effect of I/O performance on computational speed was further evaluated. According to the experimental setup listed in Table 6, the runtime was

https://doi.org/10.5194/egusphere-2026-3195
Preprint. Discussion started: 22 July 2026

17m39s when NetCDF with serial I/O was used, whereas it decreased to 15m40s when PNetCDF with parallel I/O was adopted. The advantages of asynchronous I/O were further investigated, and the results are presented in Table 10. The results in Table 10 reveal two key optimization patterns. First, there exists an optimal proportion of I/O resources. In the tests of asynchronous I/O process ratio, the best performance was obtained when the proportion of I/O processes ranged from 7.5% to 12.5%, with runtimes of 13m49s to 16m02s. Performance deteriorated when the proportion was too low (⩽5%) or too high (⩾15%), indicating that computational and I/O resources must be carefully balanced. Second, the internal grouping layout of I/O processes also had a marked effect on performance. In the asynchronous task grouping tests, the total number of I/O processes was fixed at 50, while the number of processes per group and the number of groups were varied. The optimal performance was achieved with a configuration of 25 processes per group and 2 groups, which yielded the shortest runtime of 13m38s.

To further overcome the computational performance bottleneck, asynchronous I/O was combined with the parallel I/O library PNetCDF for joint optimization. Using the previously identified optimal grouping configuration ($N_{I/O,task} = 25,\ N_{I/O,group} = 2$), additional tests were conducted. Under this combined scheme, the runtime of the 1 h fire case was reduced to 12m20s, representing an improvement of approximately 9.2% relative to the best result obtained using asynchronous I/O alone (13m38s), and 29.3% relative to the baseline serial I/O case (17m39s). These results demonstrate that the combined asynchronous I/O and PNetCDF strategy effectively alleviated the I/O bottleneck in WRF-SFIRE and provided a substantial performance gain for high-resolution and long-duration operational simulations.

4 Conclusions

This study systematically evaluated the effects of meteorological forcing, land-cover-derived fuel distribution, and key fire-related parameters on WRF-SFIRE simulations of the 1 May 2023 extreme grassland fire in Prairie Chenbarhu Banner, Inner Mongolia, and further optimized the model performance from the perspectives of compiler selection, parallel strategy, grid decomposition, and I/O configuration.

The results showed that fire–atmosphere feedback significantly enhanced the spread rate and burned area by strengthening local winds and promoting low-pressure development. Among the tested meteorological forcings, the FNL 6h-driven case achieved the best spatial agreement with the observed burn scar, with a Recall of 39.1%, whereas ERA5 was more responsive to short-term meteorological variability but tended to overestimate fire spread. Land-cover data affected the simulations mainly through their influence on fuel spatial distribution. FROM_GLC30 (2017) produced overall better agreement with the observed burned area but tended to overexpand the fire perimeter, GlobeLand30 (2020) gave more conservative results because of weaker fuel continuity, and GLC_FCS30D (2022) performed better in identifying fine-scale non-burnable patches and suppressing excessive head-fire expansion. Sensitivity experiments further indicated that wind speed was the dominant meteorological factor controlling burned area and spread distance, relative humidity mainly affected spread rate and flame length, and air temperature played a comparatively weaker role. Among fuel parameters, fuel load mainly influenced fire intensity, fuel depth dominated burned area changes, and fuel moisture primarily regulated spread rate.

The computational optimization results demonstrated that the performance of WRF-SFIRE was jointly controlled by compiler environment, process decomposition, load balance, and I/O strategy. On the Intel Xeon Gold 6148 platform, Intel 18 showed the best overall performance. Asymmetric process decomposition, 90%-95% core utilization, and hybrid MPI+OpenMP parallelization further improved runtime efficiency and reduced memory pressure. The optimized configuration, particularly the combined use of PNetCDF and asynchronous I/O, achieved an overall runtime reduction of 29.3% relative to the baseline case. These results highlight the importance of both physically realistic input representation and architecture-aware computational optimization for efficient and reliable grassland fire simulation. Future work should focus on developing localized fuel parameter datasets, quantifying coupled effects among multiple environmental factors, and improving the representation of firefighting intervention in order to enhance model realism and applicability in operational scenarios.

Data availability

The model used in this study is open source and publicly available. The WRF-SFIRE model code (WRF v4.4, SFIRE v0.1), the main data supporting the findings of this study, and the remote sensing imagery used are accessible from Zenodo: https://doi.org/10.5281/zenodo.21439181. The land cover datasets used in this study include: FROM-GLC (2017) (https://doi.org/10.1016/j.scib.2019.03.002, Gong et al., 2019), GlobeLand30 (2020) (https://doi.org/10.1080/10095020.2021.1894906, Chen et al., 2021), and GLC_FCS30D (2022) (https://doi.org/10.5194/essd-16-1353-2024, Zhang et al., 2024).

Author contributions

ML and QW conceived and organized the study. ML conducted the data analysis and drafted the manuscript. YW provided guidance on the WRF-SFIRE simulations. BZ, JT and MF provided the satellite remote sensing imagery and guidance on its processing. PG assisted with the visualization of the manuscript. HC offered suggestions for the manuscript analysis. JZ supported the development of the high-resolution model. JH provided relevant meteorological data and operational support for the Hulun Buir region. All authors read and approved the final manuscript.

Competing interests

The authors declare no competing interests.

https://doi.org/10.5194/egusphere-2026-3195
Preprint. Discussion started: 22 July 2026

Acknowledgements

We appreciate the technical support provided by the High Performance Scientific Computing Center of Beijing Normal University.

Financial support

This work was supported by the National Key R&D Program of China (2023YFC3705705).

Reference

Ager, A.A., Vaillant, N.M., Finney, M.A.: Integrating Fire Behavior Models and Geospatial Analysis for Wildland Fire Risk Assessment and Fuel Management Planning. J. Combust. 2011, 572452, https://doi.org/10.1155/2011/572452, 2011.

Anderson, H.E.: Aids to determining fuel models for estimating fire behavior. Gen Tech Rep INT-GTR-122 Ogden Utah US Department Agric. For. Serv. Intermt. For. Range Exp. Stn. 22 P 122, https://doi.org/10.2737/INT-GTR-122, 1982.

Benik, J.T., Farguell, A., Mirocha, J.D., Clements, C.B., Kochanski, A.K.: Analysis of Fire-Induced Circulations during the FireFlux2 Experiment. Fire 6, 332, https://doi.org/10.3390/fire6090332, 2023.

Burgan, R.E., Rothermel, R.C.: BEHAVE: fire behavior prediction and fuel modeling system--FUEL subsystem, General Technical Report INT-167. Ogden, UT: U. S. Department of Agriculture, Forest Service, Intermountain Forest and Range Experiment Station. 126 p, https://doi.org/10.2737/INT-GTR-167, 1984.

Cao, Y., Yin, M., Tian, J., Liang, S.: Increased summertime wildfire as a major driver of the clear-sky dimming in the Siberian Arctic from 2000 to 2020. Atmos. Res. 306, 107458, https://doi.org/10.1016/j.atmosres.2024.107458, 2024.

Chen, F., Dudhia, J.: Coupling an Advanced Land Surface-Hydrology Model with the Penn State-NCAR MM5 Modeling System. Part I: Model Implementation and Sensitivity, https://doi.org/10.1175/1520-0493(2001)129<0569:CAALSH>2.0.CO;2, 2001.

Chen, J., Chen, L., Chen, F., Ban, Y., Li, S., Han, G., Tong, X., Liu, C., Stamenova, V., Stamenov, S.: Collaborative validation of GlobeLand30: methodology and practices. Geo-Spat. Inf. Sci. 24, 134-144, https://doi.org/10.1080/10095020.2021.1894906, 2021.

Chen, Jun, Chen, Jin, Liao, A., Cao, X., Chen, L., Chen, X., He, C., Han, G., Peng, S., Lu, M., Zhang, W., Tong, X., Mills, J.: Global land cover mapping at 30 m resolution: a POK-based operational approach. ISPRS J. Photogramm. Remote Sens., Global Land Cover Mapping and Monitoring 103, 7-27, https://doi.org/10.1016/j.isprsjprs.2014.09.002, 2015.

Cheung, K.K.W., Sharples, J., Del Favero, D., Tirado Cortes, C.: Dynamic fire-atmosphere interaction in the 2020 Montana Bridger Foothills Wildfire as revealed by WRF-SFIRE simulations. Npj Nat. Hazards 2, 75, https://doi.org/10.1038/s44304-025-00132-0, 2025.

Clark, T., Coen, J., Latham, D.: Description of a coupled atmosphere-fire model. Int. J. Wildland Fire 13, 49-63, https://doi.org/10.1071/wf03043, 2004.

Deardorff, J.W.: Stratocumulus-capped mixed layers derived from a three-dimensional model. Bound.-Layer Meteorol. 18, 495-527, https://doi.org/10.1007/BF00119502, 1980.

Dudhia, J.: Numerical Study of Convection Observed during the Winter Monsoon Experiment Using a Mesoscale Two-Dimensional Model, https://doi.org/10.1175/1520-0469(1989)046<3077:NSOCOD>2.0.CO;2, 1989.

Gong, P., Liu, H., Zhang, M., Li, C., Wang, J., Huang, H., Clinton, N., Ji, L., Li, Wenyu, Bai, Y., Chen, B., Xu, B., Zhu, Z., Yuan, C., Ping Suen, H., Guo, J., Xu, N., Li, Weijia, Zhao, Y., Yang, J., Yu, C., Wang, X., Fu, H., Yu, L., Dronova, I., Hui, F., Cheng, X., Shi, X., Xiao, F., Liu, Q., Song, L.: Stable classification with limited sample: transferring a 30-m resolution sample set collected in 2015 to mapping 10-m resolution global land cover in 2017. Sci. Bull. 64, 371-373, https://doi.org/10.1016/j.scib.2019.03.002, 2019.

Hersbach, H., Bell, B., Berrisford, P., Hirahara, S., Horányi, A., Muñoz-Sabater, J., Nicolas, J., Peubey, C., Radu, R., Schepers, D., Simmons, A., Soci, C., Abdalla, S., Abellan, X., Balsamo, G., Bechtold, P., Biavati, G., Bidlot, J., Bonavita, M., De Chiara, G., Dahlgren, P., Dee, D., Diamantakis, M., Dragani, R., Flemming, J., Forbes, R., Fuentes, M., Geer, A., Haimberger, L., Healy, S., Hogan, R.J., Hólm, E., Janisková, M., Keeley, S., Laloyaux, P., Lopez, P., Lupu, C., Radnoti, G., de Rosnay, P., Rozum, I., Vamborg, F., Villaume, S., Thépaut, J.-N.: The ERA5 global reanalysis. Q. J. R. Meteorol. Soc. 146, 1999-2049, https://doi.org/10.1002/qj.3803, 2020.

Hong, S.-Y., Dudhia, J., Chen, S.-H.: A Revised Approach to Ice Microphysical Processes for the Bulk Parameterization of Clouds and Precipitation, https://doi.org/10.1175/1520-0493(2004)132<0103:ARATIM>2.0.CO;2, 2004.

Hong, S.-Y., Lim, J.: The WRF Single-Moment 6-Class Microphysics Scheme (WSM6). Asia-Pac. J. Atmos. Sci, 2006.

Hu, H., Deng, X., Zhang, G., Feng, L., Long, J., Li, Z., Zhu, Y., Wang, Y.: Fire behavior simulation of Xintian forest fire in 2022 using WRF-fire model. Front. For. Glob. Change 7, https://doi.org/10.3389/ffgc.2024.1336716, 2024.

Hu, X., Sun, Y., Ntaimo, L.: DEVS-FIRE: design and application of formal discrete event wildfire spread and suppression models. Simulation 88, 259-279, https://doi.org/10.1177/0037549711414592, 2012.

Iacono, M.J., Delamere, J.S., Mlawer, E.J., Shephard, M.W., Clough, S.A., Collins, W.D.: Radiative forcing by long-lived greenhouse gases: Calculations with the AER radiative transfer models. J. Geophys. Res. Atmospheres 113, https://doi.org/10.1029/2008JD009944, 2008.

Jiménez, P.A., Dudhia, J., González-Rouco, J.F., Navarro, J., Montávez, J.P., García-Bustamante, E.: A Revised Scheme for the WRF Surface Layer Formulation,

https://doi.org/10.5194/egusphere-2026-3195
Preprint. Discussion started: 22 July 2026

https://doi.org/10.1175/MWR-D-11-00056.1, 2012.

Kain, J.S.: The Kain-Fritsch Convective Parameterization: An Update, https://doi.org/10.1175/1520-0450(2004)043<0170:TKCPAU>2.0.CO;2, 2004.

Kochanski, A.K., Jenkins, M.A., Mandel, J., Beezley, J.D., Clements, C.B., Krueger, S.: Evaluation of WRF-SFIRE performance with field observations from the FireFlux experiment. Geosci. Model Dev. 6, 1109-1126, https://doi.org/10.5194/gmd-6-1109-2013, 2013.

Lai, S., Chen, H., He, F., Wu, W.: Sensitivity experiments of the local wildland fire with WRF-fire module. Asia-Pac. J. Atmos. Sci. 56, 533-547, https://doi.org/10.1007/s13143-019-00160-7, 2020.

Lilly, D.K.: On the numerical simulation of buoyant convection. Tellus 14, 148-172, https://doi.org/10.1111/j.2153-3490.1962.tb00128.x, 1962.

Linn, R., Reisner, J., Colman, J.J., Winterkamp, J.: Studying wildfire behavior using FIRETEC. Int. J. Wildland Fire 11, 233-246, https://doi.org/10.3402/tellusa.v14i2.9537, 2002.

Liu, Y., Miao, S., Zhang, H.: Sensitivity simulations of the 30 march 2020 xichang wildfire in southwest China based on the WRF-fire model. J. Meteorol. Res. 38, 826-843, https://doi.org/10.1007/s13351-024-3171-5, 2024.

Mallia, D.V., White, C., Farguell, A., Mandel, J., Kochanski, A.K.: Simulating the impacts of regional wildfire smoke on ozone using a coupled fire-atmosphere-chemistry model. Atmos. Environ. 360, 121404, https://doi.org/10.1016/j.atmosenv.2025.121404, 2025.

Mandel, J., Amram, S., Beezley, J.D., Kelman, G., Kochanski, A.K., Kondratenko, V.Y., Lynn, B.H., Regev, B., Vejmelka, M.: Recent advances and applications of WRF-SFIRE. Nat. Hazards Earth Syst. Sci. 14, 2829-2845, https://doi.org/10.5194/nhess-14-2829-2014, 2014.

Mandel, J., Beezley, J.D., Kochanski, A.K.: Coupled atmosphere-wildland fire modeling with WRF 3.3 and SFIRE 2011. Geosci. Model Dev. 4, 591-610, https://doi.org/10.5194/gmd-4-591-2011, 2011.

National Centers for Environmental Prediction, National Weather Service, NOAA, U.S. Department of Commerce: NCEP GDAS/FNL 0.25 degree global tropospheric analyses and forecast grids, https://doi.org/10.5065/D65Q4T4Z, 2015.

Patton, E.G., Coen, J.L.: WRF-Fire: A Coupled Atmosphere-Fire Module for WRF, 2004.

Smagorinsky, J.: General circulation experiments with the primitive equations. Mon. Weather Rev. 91, 99-164, https://doi.org/10.1175/1520-0493(1963)091<0099:GCEWTP>2.3.CO;2, 1963.

Li, Y.: A Study on Near-Surface Wind and Forest Fire Simulation in Liangshan, Sichuan. Nanjing University of Information Science and Technology, https://doi.org/10.27248/d.cnki.gnjqc.2023.001638, 2023.

Wang, Y., Shi, L., Shi, Z., Yao, Q., Wang, Z., Zhong, L.: Assessing the fire-modified meteorology of the grassland and forest intersection zone in Mongolia using the

https://doi.org/10.5194/egusphere-2026-3195
Preprint. Discussion started: 22 July 2026

WRF-fire model. Fire 6, 443, https://doi.org/10.3390/fire6110443, 2023.
Wang, Z.: CURRENT FOREST FIRE DANGER RATING SYSTEM. J. Nat. Disasters 39-44, 1992.
Yang, J., Dong, Q.: Simulation of the evolution of the 21 May 2009 wildfire from Mongolia to China using WRF-Fire Model. Trans Atmos Sci 43, 718-727, https://doi.org/10.13878/j.cnki.dqkxxb.20170418001, 2020.
Zhang, J., Liu, B., Chu, T., Di, X., Jin, S.: Fire behavior of ground surface fuels in Pinus koraiensis and Quercus mongolica mixed forest under no wind and zero slope condition:A prediction with extended Rothermel model. Chin. J. Appl. Ecol. 1495-1502, https://doi.org/10.1007/s11783-011-0280-z, 2012.
Zhang, X., Zhao, T., Xu, H., Liu, W., Wang, J., Chen, X., Liu, L.: GLC_FCS30D: the first global 30m land-cover dynamics monitoring product with a fine classification system for the period from 1985 to 2022 generated using dense-time-series landsat imagery and the continuous change-detection method. Earth Syst. Sci. Data 16, 1353-1381, https://doi.org/10.5194/essd-16-1353-2024, 2024.
Zhou H., Wang Y., Zhou G.-S.: Temporal and spatial dynamics of grassland fires in Inner Mongolia. Acta Prataculturae Sin. 25, 16-25, https://doi.org/10.11686/cyxb2015286, 2016.
Zhou N., Li X., Zhao F., Si L., Wang M., Li Weike, Yan K., Li Wei: Simulation of behavior of the Chenbalhu Banner grassland fire using BehavePlus. Pratacultural Sci. 42, 2392-2402, https://doi.org/10.11829/j.issn.1001-0629.2024-0325, 2025.